magnetochemistry

MDPI

Article

Strain-Driven Reorganisation of Competing Exchange Interactions and Anomalous Tuning of the Magnetic Ordering Temperature in Monolayer $MnSb_2Te_4$

Tuan-Anh Tran [1,*], Ngoc Toan Dang [2,3,*], Le Van Thanh Nguyen [1], Son Hai Le [1], Hai Cat Tran [1], Ngoc Loan Phan [4] and Denis P. Kozlenko [5]

[1] Department of Engineering Physics, Faculty of Applied Sciences, Ho Chi Minh City University of Technology and Engineering, Ho Chi Minh City 700000, Vietnam
[2] Faculty of Natural Sciences, Duy Tan University, Da Nang 550000, Vietnam
[3] Institute of Research and Development, Duy Tan University, Da Nang 550000, Vietnam
[4] Department of Physics, Ho Chi Minh City University of Education, Ho Chi Minh City 700000, Vietnam
[5] Frank Laboratory of Neutron Physics, Joint Institute for Nuclear Research, Dubna 141980, Russia
* Correspondence: anhtt@hcmute.edu.vn (T.-A.T.); dangngoctoan1@duytan.edu.vn (N.T.D.)

Abstract

Lattice strain is generally considered an effective instrument for tuning magnetism in two-dimensional materials, although its influence on competing exchange interactions remains insufficiently understood. Here, density functional theory calculations with strain-dependent, linear-response Hubbard parameters, complemented by fixed-U calculations, reveal a pronounced reorganisation of the magnetic exchange hierarchy in monolayer $MnSb_2Te_4$ under biaxial strain. The nearest-neighbour ferromagnetic interaction shows a complex non-monotonic response: it increases under compression from −5% to −2%, passes through a broad maximum between −2% and 0%, and decreases rapidly under tension up to +5%. In contrast, the effective next-nearest-neighbour interaction is progressively suppressed and eventually reverses sign. These changes cannot be explained by the smooth evolution of individual structural or electronic descriptors. Instead, comparison of the two correlation treatments reveals competing contributions with distinct strain dependences: the tensile suppression of the net ferromagnetic exchange is primarily associated with a growing antiferromagnetic contribution that follows the Goodenough–Kanamori–Anderson angular dependence. Classical Monte Carlo simulations with easy-axis single-ion anisotropy show that the magnetic ordering temperature is maximal between −2% and 0%, qualitatively resembling the nearest-neighbour exchange but varying much more strongly. Strain-controlled magnetism in monolayer $MnSb_2Te_4$ is thus governed by the whole hierarchy of competing exchange interactions.

Keywords: $MnSb_2Te_4$; two-dimensional magnetism; biaxial strain; exchange interactions; DFT + U; linear-response Hubbard U; superexchange; Monte Carlo; Curie temperature

Check for updates

Academic Editor: Carlos J. Gómez García

Received: 3 November 2026
Revised: 12 November 2026
Accepted: 16 November 2026
Published: 18 November 2026

Copyright: © 2026 by the authors. Licensee MDPI, Basel, Switzerland. This article is an open access article distributed under the terms and conditions of the Creative Commons Attribution (CC BY) license.

1. Introduction

Strain engineering provides a promising and versatile route for controlling magnetic interactions in two-dimensional (2D) materials [1–4]. Mechanical deformation can alter the balance between in-plane exchange interactions of ferromagnetic (FM) and antiferromagnetic (AFM) nature by changing interatomic distances and bond angles and thereby modifying orbital overlap [3,4]. While strain-induced changes in magnetism are often interpreted in terms of variations in the magnitude of a single effective exchange

constant, this description may become insufficient when multiple exchange pathways contribute simultaneously and respond differently to structural deformation. In such systems, the interplay of strain-controlled competing interactions can produce an unusually complex response of the magnetic and associated physical properties, caused by substantial changes in the underlying exchange hierarchy. Understanding how competing exchange pathways evolve under strain is thus essential for establishing a microscopic picture of strain-controlled magnetism.

The layered Mn-based chalcogenide family provides an ideal platform for exploring this problem. Compounds such as $MnBi_2Te_4$ have attracted considerable interest because magnetic order is coupled to non-trivial electronic topology, giving rise to challenging phenomena including axion-insulator and quantum anomalous Hall states [5–7]. In this family, the magnetic configuration is closely connected to the features of the electronic structure, making the control of magnetic interactions an important consideration for potential spintronic and topological applications. However, the magnetic properties are also sensitive to structural imperfections and chemical disorder. In particular, Mn/Sb site mixing in $MnSb_2Te_4$ has been shown to influence its magnetic ground state and interlayer exchange interactions [8–10]. These findings highlight the need to distinguish intrinsic magnetic interactions from effects associated with disorder and to understand how the exchange network responds to controlled structural perturbations.

Monolayer $MnSb_2Te_4$ offers a convenient theoretical setting for clarifying the intrinsic response of the in-plane exchange interactions to mechanical deformation. In the ideal, stoichiometric monolayer considered here, the Mn atoms form a triangular lattice in which the nearest-neighbour ferromagnetic interaction competes with the next-nearest-neighbour (second-shell) interaction, which is predominantly antiferromagnetic, as also found for the closely related compound $MnBi_2Te_4$ [11]. The system is well suited to this problem because the Mn^{2+} ions carry localised high-spin d^5 moments and neighbouring Mn ions are connected through Mn–Te–Mn bonds with angles close to 90°, a geometry in which ferromagnetic and antiferromagnetic exchange contributions can compete sensitively. In addition, the ideal stoichiometric monolayer excludes the site mixing that complicates the interpretation of bulk samples. Biaxial strain modifies the balance of these competing interactions through changes in the local bonding geometry and electronic structure, which controls the nature of the magnetic ground state and its modifications.

A further consideration is the treatment of electronic correlation in first-principles calculations. The magnetic exchange interactions of transition-metal compounds are sensitive to the description of localised d electrons, for which the DFT + U approach is widely employed. In many strain-dependent studies, the Hubbard parameter U is held fixed throughout the structural deformation, implicitly assuming that changes in the effective correlation strength do not qualitatively affect the predicted magnetic response. Recent diffusion Monte Carlo calculations for monolayer $MnBi_2Te_4$, however, have demonstrated that the optimal effective U depends on strain and that the predicted magnetic behaviour can be sensitive to its choice [12]. Although $MnBi_2Te_4$ and $MnSb_2Te_4$ are distinct compounds, this result motivates an explicit examination of correlation effects in strain-dependent calculations of the latter. Determining U independently at each strain using the linear-response method of Cococcioni and de Gironcoli [13], while retaining a fixed-U reference calculation, provides a way to assess the robustness of the predicted exchange trends and to investigate their sensitivity to electronic correlation. Importantly, the comparison between these two computational treatments can provide insight beyond the conventional assessment of parameter sensitivity, since different microscopic contributions to magnetic exchange may depend differently on U [14,15], although such a comparison yields a phenomenological rather than a unique microscopic separation.

In this work, we investigate the strain dependence of the structural, electronic, and magnetic properties of ideal monolayer $MnSb_2Te_4$ using density functional theory with both a linear-response, strain-dependent U and a fixed-U reference. We map the calculated energies of selected collinear magnetic configurations onto an effective two-shell Heisenberg model and examine the resulting exchange interactions alongside structural parameters, local electronic descriptors, and ligand spin polarisation. We then use the distinct U-dependence of the two computational branches to investigate the competing contributions to the exchange interactions and assess their relationship with the bonding geometry within the Goodenough–Kanamori–Anderson framework [14–17]. Finally, classical Monte Carlo simulations incorporating easy-axis single-ion anisotropy, held fixed with strain, are employed to examine how the strain-dependent exchange hierarchy influences the magnetic ordering temperature. We also discuss the applicability and limitations of this approach for other low-dimensional magnets.

We show that biaxial strain produces an unexpectedly complex response of the competing nearest-neighbour and next-nearest-neighbour exchange interactions in monolayer $MnSb_2Te_4$, a reorganisation of their hierarchy, and an unusual strain dependence of the magnetic ordering temperature.

2. Computational Methods

2.1. First-Principles Calculations and Strain-Dependent Hubbard Parameter

First-principles calculations were performed within density functional theory (DFT) using the Quantum ESPRESSO package [18,19]. The exchange–correlation energy was described by the Perdew–Burke–Ernzerhof (PBE) functional [20], together with projector augmented-wave datasets [21], the D3 dispersion correction [22], and the Dudarev formulation of DFT + U [23]. A rectangular supercell containing 28 atoms (4 Mn, 8 Sb, and 16 Te) was employed throughout the calculations.

Biaxial strain was introduced by uniformly scaling the two in-plane lattice vectors according to

$$\varepsilon = \frac{a - a_0}{a_0}, \tag{1}$$

where a_0 and a denote the unstrained and strained in-plane lattice parameters, respectively. The unstrained lattice parameter, $a_0 = 4.279$ Å, was obtained from a variable-cell relaxation of the monolayer in which only the in-plane lattice vectors were allowed to change; it is 0.4% larger than the experimental bulk value of 4.2613 Å [24]. Strains from −5% to +5% were considered in steps of 1%. At each strain, the in-plane lattice vectors and the cell height were kept fixed, and all atomic positions were relaxed until the residual forces fell below 10^{-3} Ry bohr^{-1} and the change in total energy between ionic steps fell below 10^{-5} Ry. Each magnetic configuration and each Hubbard branch (see below) was relaxed separately. The plane-wave and charge-density cutoffs were 60 and 600 Ry, respectively, the self-consistency threshold was 10^{-8} Ry, Gaussian smearing of 0.01 Ry was used, and the Brillouin zone of the rectangular cell was sampled with a 12 × 4 × 1 Monkhorst–Pack mesh. The cell height of 41 Å provides a vacuum region exceeding 30 Å, and two-dimensional electrostatic decoupling was applied to suppress spurious interactions between periodic images [25]. Identical numerical settings were used throughout the strain series.

To assess the role of electronic correlation, two computational branches were considered. In the first, the Hubbard parameter was determined independently at each strain using the linear-response approach of Cococcioni and de Gironcoli [13], in its supercell formulation. A 2 × 2 hexagonal supercell (28 atoms, four Mn) in the ferromagnetic state was used, with a 6 × 6 × 1 k-point mesh; localised potential shifts $\alpha = \pm 0.05$ and ± 0.10 eV were applied to the 3d manifold of one Mn atom, starting from the $U \approx 0$ ground state, and the resulting

change in its 3d occupation (atomic projectors) was recorded before and after self-consistent screening, giving the bare response χ_0 and the screened response χ. The perturbed Mn atom and its periodic images are separated by $2a \approx 8.6$ Å. The Hubbard parameter is then obtained as

$$U(\varepsilon) = \chi_0^{-1} - \chi^{-1}. \quad (2)$$

Repeating this procedure at every strain yields the strain-dependent, linear-response $U(\varepsilon)$ (Figure 1). The procedure was applied once at each strain rather than iterated to self-consistency in U. In the second branch, the same calculations were repeated with a fixed Hubbard parameter of $U = 3$ eV. Because each branch was relaxed with its own U, the geometries of the two branches differ slightly (Mn–Te bond lengths by at most 0.003 Å and Mn–Te–Mn angles by at most 0.13°); the difference between the branches is therefore dominated by the change in U but also contains a small geometric contribution. As discussed in Section 3.3, the contrasting U-dependence of the two branches is used to investigate the competing contributions to the nearest-neighbour exchange interaction.

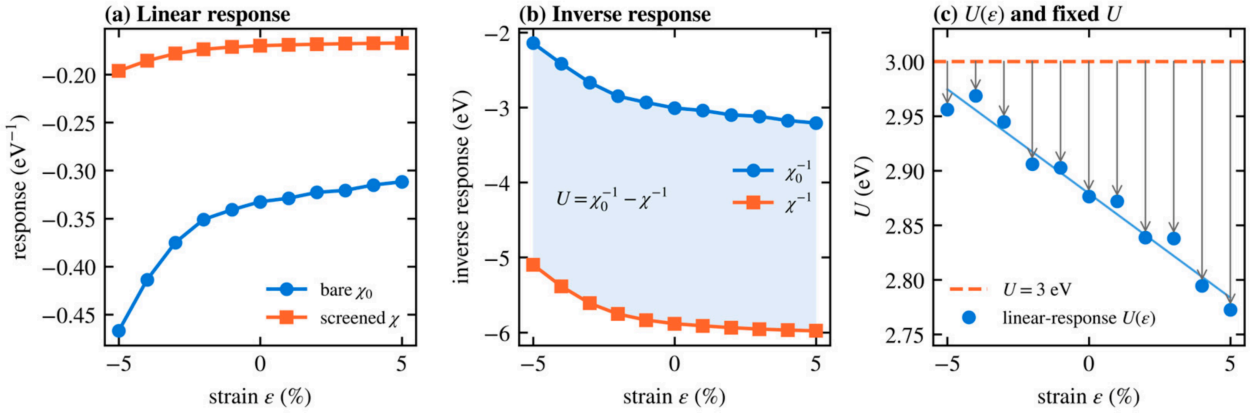


Figure 1. Linear-response determination of the Hubbard parameter. (**a**) Bare (χ_0) and screened (χ) responses of the Mn 3d occupation to the applied perturbation. (**b**) Their inverses; $U = {\chi_0}^{-1} - \chi^{-1}$ is the separation between the two curves (shaded). (**c**) The resulting linear-response $U(\varepsilon)$, which decreases by 6.2% almost linearly ($R^2 = 0.97$), compared with the fixed $U = 3$ eV branch; arrows mark $\Delta U = U(\varepsilon) - 3$ eV, which is smallest under compression.

2.2. Mapping of Magnetic Exchange Interactions

The magnetic exchange interactions were extracted by mapping the total energies of selected collinear magnetic configurations onto a classical two-shell Heisenberg Hamiltonian defined on the triangular Mn lattice:

$$H = -\sum_{\langle ij \rangle} J_1 \, \mathbf{S}_i \cdot \mathbf{S}_j - \sum_{\langle\langle ij \rangle\rangle} J_2 \, \mathbf{S}_i \cdot \mathbf{S}_j, \quad (3)$$

where J_1 and J_2 represent the nearest-neighbour and effective second-shell (next-nearest-neighbour) exchange interactions, respectively. Each pair is counted once (so that the energy per Mn of the ferromagnetic state is $-3S^2(J_1 + J_2)$), and positive and negative exchange constants correspond to ferromagnetic and antiferromagnetic coupling, respectively. The classical spin magnitude was set to $S = 5/2$, consistent with the nominal high-spin Mn^{2+} configuration.

Three collinear magnetic configurations—ferromagnetic, stripy, and zigzag—were considered to determine the two exchange parameters. The energy differences between the stripy and ferromagnetic configurations and between the zigzag and ferromagnetic configurations are, per Mn atom, given by

$$\Delta E_{ST} = 4S^2J_1 + 4S^2J_2 \quad (4)$$

and

$$\Delta E_{ZZ} = 2S^2J_1 + 4S^2J_2, \quad (5)$$

respectively. Subtracting these expressions eliminates the second-shell contribution, giving

$$J_1 = \frac{\Delta E_{ST} - \Delta E_{ZZ}}{2S^2}. \quad (6)$$

The second-shell parameter then follows from either energy difference. Because the total-energy differences directly determine the combinations S^2J_i, the exchange interactions are reported as S^2J_i in meV; the energy differences and exchange parameters at each strain are listed in Table 1. The self-consistency threshold corresponds to an uncertainty well below 0.001 meV in each S^2J_i; the dominant numerical uncertainty arises instead from the separate relaxation of the configurations. We therefore assign an uncertainty of 0.002 meV to each S^2J_i. This estimate is consistent with the scatter of the difference between the two Hubbard branches about a smooth curve (root-mean-square deviation of approximately 0.004 meV for S^2J_1).

Table 1. Lattice parameter a, Mn–Te–Mn bridging angle θ, linear-response Hubbard parameter $U(\varepsilon)$, magnetic energy differences per Mn, exchange parameters, and anisotropic Heisenberg ordering temperature of monolayer $MnSb_2Te_4$ under biaxial strain ($U(\varepsilon)$ branch).

ε (%)	a (Å)	θ (°)	U (eV)	ΔE_{ST} (meV)	ΔE_{ZZ} (meV)	S^2J_1 (meV)	S^2J_2 (meV)	T_C (K)
−5	4.065	89.65	2.956	3.516	0.841	1.337	−0.458	5.7
−4	4.107	90.40	2.969	4.464	1.488	1.488	−0.372	10.4
−3	4.150	91.15	2.945	4.966	1.823	1.572	−0.330	12.4
−2	4.193	91.91	2.906	5.133	1.943	1.595	−0.312	13.3
−1	4.236	92.63	2.903	5.141	1.978	1.582	−0.296	13.8
0	4.279	93.30	2.876	5.110	1.972	1.569	−0.291	13.2
+1	4.321	94.08	2.872	4.591	1.759	1.416	−0.268	12.0
+2	4.364	94.81	2.839	4.096	1.564	1.266	−0.242	10.9
+3	4.407	95.53	2.838	3.592	1.421	1.086	−0.188	10.1
+4	4.450	96.27	2.795	2.939	1.258	0.841	−0.106	9.0
+5	4.492	97.00	2.772	2.296	1.184	0.556	0.018	8.3

The same energy relations also provide a useful connection between the correlation dependence of the total energies and that of J_1. Defining the energy slopes $k_{ST} = \Delta(\Delta E_{ST})/\Delta U$ and $k_{ZZ} = \Delta(\Delta E_{ZZ})/\Delta U$, where Δ denotes the difference between the linear-response and fixed-U calculations at a given strain, the two-shell model gives

$$k_{ST} - k_{ZZ} = 2S^2\frac{\Delta J_1}{\Delta U}. \quad (7)$$

Equation (7) shows that the U-dependence of J_1 is determined by the stripy and zigzag energy slopes alone, without reference to J_2. It follows from the bond-counting relations for the selected configurations within the two-shell model and is not a general identity for exchange Hamiltonians containing additional interaction shells or anisotropic terms.

The two-shell mapping should be interpreted as an effective description of the magnetic energy landscape rather than a unique determination of all microscopic exchange pathways. Since only three collinear configurations are used to determine two exchange parameters, interactions beyond the second shell cannot be resolved independently and may contribute to the extracted J_2. Accordingly, J_2 is referred to throughout this work as an effective second-shell interaction. Its value should not be interpreted as an unambiguous microscopic next-nearest-neighbour exchange constant. Since longer-range interactions cannot be resolved

independently within the present mapping, the extracted J_2 may incorporate contributions beyond the genuine second-shell coupling, and its magnitude does not provide a model-independent bound on that coupling.

2.3. Structural and Electronic Descriptors

To investigate the microscopic origin of the strain-dependent exchange interactions, several structural and electronic descriptors were examined alongside J_1 and J_2. These included the Mn–Te bond length, the Mn–Te–Mn bond angle, the Mn–Mn separation distance, the Hubbard parameter, the Mn Bader charge, and the real-space spin density.

Bader charge analysis was performed using the converged charge density [26–28]. Numerical consistency was assessed by examining the integrated charge and spin density, as well as the differences between symmetry-equivalent atomic sites. The total Bader charge reproduced the valence-electron count to within approximately one part in 10^4, while the integrated spin density agreed with the calculated magnetic moment to better than 0.05%. Symmetry-equivalent sites provided an internal estimate of numerical noise; for the Bader charges, the typical scatter was approximately 2×10^{-4} e. Changes in the local descriptors were therefore interpreted as physically meaningful only when they exceeded the corresponding numerical uncertainty by a sufficient margin, approximately three times the estimated noise level.

The combined analysis of these quantities was used to determine whether the non-monotonic exchange response could be associated with a single structural or electronic variable, or whether it instead reflected competition between contributions with different strain dependences.

2.4. Monte Carlo Simulations of Magnetic Ordering

The strain-dependent exchange parameters were used in classical Monte Carlo simulations on the triangular Mn lattice with periodic boundary conditions. Two magnetic models were considered: the Ising limit, representing the reference case of infinitely strong easy-axis anisotropy, and an anisotropic Heisenberg model of classical unit vectors incorporating a finite single-ion anisotropy. Both models use the Hamiltonian of Equation (3) with the calculated S^2J_1 and S^2J_2, each pair being counted once.

Single-spin Metropolis updates were used for both models; for the Heisenberg model, each Metropolis sweep was followed by an over-relaxation sweep in which each spin is reflected about its local exchange field and the move is accepted according to the change in anisotropy energy. Simulations were performed by heating from the fully ordered state, with 2000 thermalisation sweeps and 10,000 measurement sweeps at each temperature, on lattices with $L = 24$ and $L = 48$. The ordering temperature, T_C, was determined from the crossing of the Binder cumulant of the out-of-plane magnetisation, $B_4 = 1 - \langle {m_z}^4 \rangle / (3\langle {m_z}^2 \rangle^2)$, for the two lattice sizes.

Two independent random seeds were used for each strain; the two estimates of T_C differ by 0.22 K on average (at most 0.60 K). The susceptibility maximum for $L = 48$ gives values within 0.7 K of the Binder-cumulant estimates. For comparison, a classical mean-field estimate for the Heisenberg model, $k_B T_{MF} = (z_1 J_1 + z_2 J_2) S^2/3 = 2S^2(J_1 + J_2)$ with $z_1 = z_2 = 6$, was also evaluated.

A finite ordering temperature in a two-dimensional isotropic Heisenberg model is prohibited by the Mermin–Wagner theorem [29]. Magnetic anisotropy must therefore be included to describe finite-temperature ordering in the present two-dimensional system [30]. We adopted the published easy-axis single-ion anisotropy of monolayer $MnSb_2Te_4$, $A = -0.16$ meV, which was obtained with the same pair convention and with the spin length absorbed into the parameters, and which was attributed to the combined

spin–orbit coupling of Mn and Te [31]. In the Monte Carlo Hamiltonian, the anisotropy term was written as

$$H_{\mathrm{ani}} = -D\sum_{i}(n_i^z)^2, \tag{8}$$

where $n_i{}^z$ is the out-of-plane component of the unit vector describing the orientation of spin i, and $D = |A| = 0.16$ meV. The finite-anisotropy Heisenberg results were compared with the Ising limit to assess the influence of anisotropy on the predicted ordering behaviour.

As a check of the implementation, the same procedure was applied to the published exchange and anisotropy parameters of monolayer $MnBi_2Te_4$ [31], giving $T_C = 18.1$ K, compared with the value of approximately 20 K reported in that work. This comparison tests the simulation procedure rather than the present exchange parameters.

2.5. Scope and Limitations

The first-principles calculations were performed within the scalar-relativistic approximation. Consequently, strain-dependent magnetocrystalline anisotropy energies, anisotropic exchange interactions, and band-topological properties were not evaluated explicitly. The anisotropy used in the Monte Carlo simulations was taken from previously published DFT + U + spin–orbit-coupling calculations [31] and was assumed to remain constant throughout the strain series. The resulting simulations therefore describe the influence of the calculated isotropic exchange interactions on magnetic ordering in the presence of a prescribed easy-axis anisotropy, rather than providing fully first-principles predictions of the strain-dependent transition temperature.

Furthermore, the calculations describe an ideal, stoichiometric, defect-free monolayer and do not include interlayer exchange or Mn/Sb site disorder. The predicted exchange parameters and ordering temperatures should therefore be interpreted as clean-limit theoretical results that isolate the intrinsic response of the monolayer to biaxial strain, rather than as direct quantitative predictions for experimentally realised samples. In addition, the two-shell mapping cannot resolve third-neighbour or anisotropic exchange interactions, which on the triangular lattice may be absorbed into the effective J_1 and J_2. Such contributions may become relevant near the sign change of the effective J_2 under tension, which should therefore not be taken as an unambiguous reversal of the microscopic second-neighbour coupling.

3. Results and Discussion

3.1. Strain-Driven Reorganisation of Exchange Interactions

The calculated exchange interactions reveal that biaxial strain does not simply rescale the magnetic energy landscape of monolayer $MnSb_2Te_4$ (Figure 2 and Table 1). The nearest-neighbour interaction J_1 remains ferromagnetic but shows a surprisingly complex, non-monotonic strain response. In the linear-response $U(\varepsilon)$ branch, S^2J_1 increases progressively under compression, from 1.337 meV at $\varepsilon = -5\%$ to a maximum of 1.595 meV at $\varepsilon = -2\%$. It then decreases only weakly, to 1.569 meV, on approaching the unstrained state ($\varepsilon = 0\%$). In contrast, tensile strain up to +5% produces a pronounced progressive decrease of S^2J_1, to 0.556 meV. The fixed-U calculations reproduce the same overall behaviour, demonstrating that the result is robust against the choice of Hubbard parameter and its strain variation. The microscopic mechanisms responsible for this strain response of J_1 are discussed in Section 3.3.

The effective next-nearest-neighbour interaction J_2 is antiferromagnetic under compressive strain, and its magnitude becomes progressively smaller from −5% to +4%, until it changes sign between +4% and +5% in both computational branches (Figure 2b). The sign reversal occurs well beyond the estimated numerical uncertainty of the energy mapping.

The ratio of the absolute values of the two interactions, $|J_2/J_1|$, decreases by about an order of magnitude, from 0.34 to 0.03, across the strain range (Figure 2c), indicating the diminishing role of the effective second-shell interaction. As a result, the overall exchange-energy scale $S^2(J_1 + J_2)$ remains positive and shows a broad maximum between −2% and 0% (Figure 2d), qualitatively resembling the strain dependence of J_1 but reduced by the opposite J_2 contribution, most strongly under large compressive strain. Consequently, the ferromagnetic configuration remains the lowest-energy collinear state among those considered at every strain, despite the change in sign of J_2 above +4%.

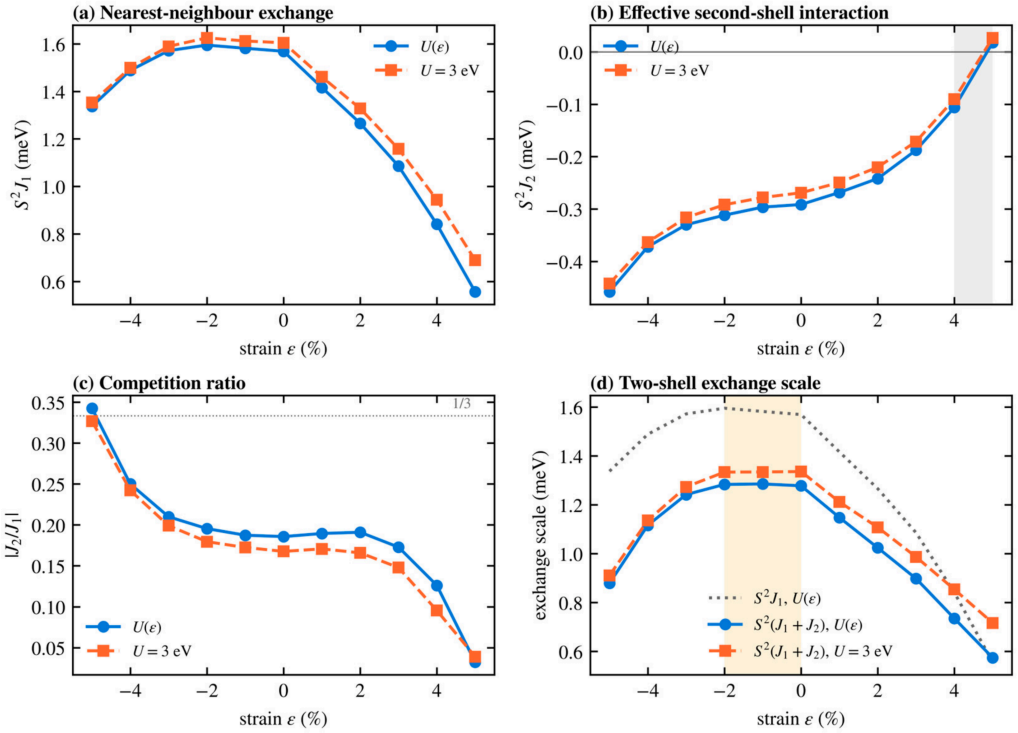


Figure 2. Strain-driven reorganisation of the exchange interactions in monolayer $MnSb_2Te_4$. (**a**) Nearest-neighbour exchange interaction (S^2J_1) calculated with the linear-response $U(\varepsilon)$ and fixed $U = 3$ eV, showing a pronounced non-monotonic response and a maximum near −2% strain. (**b**) Effective second-shell interaction (S^2J_2), which is predominantly antiferromagnetic but changes sign between +4% and +5% (shaded). (**c**) Relative strength of the competing interaction, expressed as $|J_2/J_1|$; the dotted line marks the classical stability limit 1/3 of the collinear ferromagnetic state. (**d**) Combined exchange-energy scale $S^2(J_1 + J_2)$, accounting for the partial compensation between the weakening nearest-neighbour interaction and the suppression of the competing second-shell contribution (shaded window, −2% to 0%).

3.2. Structural and Electronic Response

From compression to tension, the relaxed structures show a nearly linear increase in the Mn–Te bond length, the Mn–Mn separation, and the Mn–Te–Mn bond angle (Figure 3a–c). The variation in this angle is of particular importance because it controls the balance between ferromagnetic and antiferromagnetic contributions in ligand-mediated exchange. Within the Goodenough–Kanamori–Anderson (GKA) framework, the exchange interaction depends on the geometry of the magnetic cation–ligand–cation pathway, and its character may change between FM and AFM in the vicinity of 90° [14–17]. In the present system, the bond angle increases from 89.65° at −5% to 97.00° at +5%, passing through 90° between −5% and −4% (Figure 3b). Although J_1 remains ferromagnetic throughout, it reaches its maximum at an angle of about 91.9°, whereas it is smallest at the compressive end, where the angle is closest to 90°. A single-channel interpretation of the total exchange

based solely on the conventional angular dependence would therefore fail to reproduce the observed strain response of the nearest-neighbour interaction. This discrepancy suggests that the total interaction reflects the superposition of competing contributions with different structural dependences.

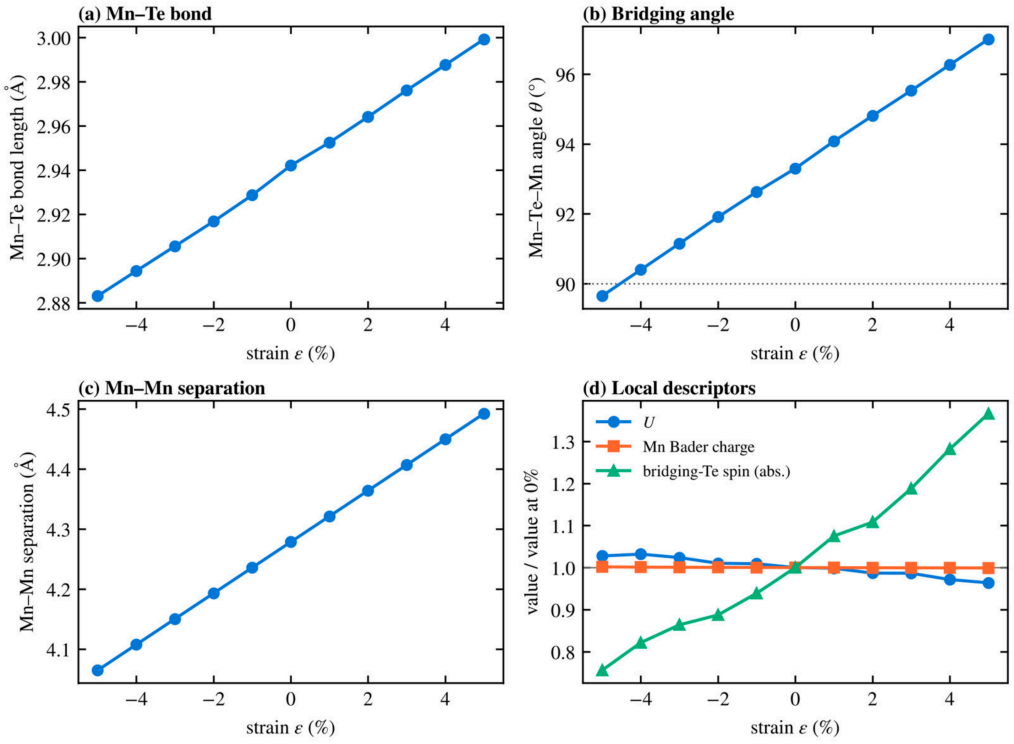


Figure 3. Structural and local electronic responses of monolayer $MnSb_2Te_4$ to biaxial strain. (**a**) Mn–Te bond length, (**b**) Mn–Te–Mn bond angle (dotted line: 90°), and (**c**) Mn–Mn separation, showing smooth and approximately linear variations with strain. (**d**) Strain dependence of the Hubbard parameter, Mn Bader charge, and bridging-Te spin polarisation, normalised to their respective values at zero strain. Unlike the exchange interaction, these local descriptors evolve smoothly across the investigated strain range.

The strain responses of the local electronic descriptors likewise show no anomalous features (Figure 3d). The Mn Bader charge remains almost constant, changing by only 0.037 e (of approximately 14.1 e) across the full strain range, while the Mn 3d occupation matrix remains smooth and consistent with the equivalence of symmetry-related sites. The Hubbard parameter also evolves smoothly, changing by only 6.2% over the same interval, and the magnitude of the spin polarisation of the bridging Te atoms increases monotonically from compression to tension. These results imply the absence of any substantial strain-induced change in the local structural and electronic descriptors that could account for the non-monotonic behaviour of J_1.

Because total-energy mapping determines only the net exchange, the comparison between the linear-response and fixed-U calculations is used in the following section to examine the competing contributions.

3.3. Exchange Mechanism

The considerations above indicate that the non-monotonic strain dependence of J_1 cannot be explained by a single structural or electronic descriptor. To investigate its origin, we exploit the different Hubbard-parameter dependences of the two computational branches. Because the two branches have nearly identical geometries at each strain (Section 2.1), their

difference provides an estimate of the sensitivity of the exchange interaction to electronic correlation. Combined with the energy-mapping relation established in Section 2.2, this comparison offers a tool for probing competing contributions that cannot be separated directly from the total exchange.

The physical interpretation of this correlation sensitivity is based on the contrasting U-dependences expected for different exchange mechanisms. In Anderson's superexchange framework, the kinetic antiferromagnetic contribution associated with virtual charge fluctuations scales approximately as $4t^2/U$, where t is the relevant hopping amplitude [14,15]. By contrast, a ferromagnetic contribution dominated by other mechanisms can be treated as nearly independent of U over the narrow interval of U investigated here. Within this phenomenological description, and with the sign convention of Equation (3), in which antiferromagnetic couplings are negative, the nearest-neighbour interaction can be written as

$$J_1 = J_{\mathrm{FM}} + J_{\mathrm{AFM}}, \tag{9}$$

with

$$J_{\mathrm{AFM}} \propto -U^{-1}, \tag{10}$$

where $J_{\mathrm{FM}} > 0$ and $J_{\mathrm{AFM}} < 0$. Since J_{FM} is approximately U-independent, the finite difference between the two calculations gives

$$J_{\mathrm{AFM}} = -U\frac{\Delta J_1}{\Delta U}, \qquad J_{\mathrm{FM}} = J_1 - J_{\mathrm{AFM}}. \tag{11}$$

The contrasting correlation dependence of ferromagnetic and antiferromagnetic interactions has also been observed in a high-throughput DFT + U study of two-dimensional materials, in which a comparison of exchange couplings for 138 magnetic monolayers revealed a systematic suppression of antiferromagnetic interactions by the Hubbard correction, without a similar trend for ferromagnetic interactions [32]. A separate DFT + U study of monolayer MnO_2 found that the nearest-neighbour ferromagnetic exchange increases approximately linearly with U [33], as expected when an antiferromagnetic kinetic contribution is progressively suppressed. These studies support the use of correlation sensitivity as a probe of competing exchange contributions, although they do not independently establish the microscopic decomposition adopted here.

An important qualification is that the calculations directly constrain $U\,\Delta J_1/\Delta U$, not a uniquely defined microscopic antiferromagnetic exchange pathway. Identifying this quantity with J_{AFM} requires the assumed inverse-U scaling, while the extraction of the derivative from the two computational branches involves a finite difference. Because only two values of U are available at each strain, the local linearity of $J_1(U)$ over the interval $\Delta U \leq 0.23$ eV is assumed rather than tested; calculations at intermediate values of U would provide a direct check. Accordingly, J_{AFM} and J_{FM} should be treated as effective parameters of the present approach, which may differ from a model-independent decomposition of the microscopic exchange Hamiltonian.

The resulting decomposition (Figure 4a), obtained from the finite-difference slope $\Delta(S^2J_1)/\Delta U$ (Figure 5c), reveals a weakly varying ferromagnetic contribution, S^2J_{FM}, which stays within 2.18–2.53 meV (a variation of about 14%) and decreases slowly under tension. The strain response of S^2J_{AFM} is more complex. Its magnitude first decreases, from about -1.10 meV at -5% to -0.83 meV at 0%, and then nearly doubles under tension, reaching about -1.63 meV at $+5\%$. The growing antiferromagnetic contribution therefore provides the major part of the tensile suppression of the net ferromagnetic interaction.

The reliability of this decomposition depends on the separation between the Hubbard parameters used in the two branches. Under compression, the difference between $U(\varepsilon)$ and the reference value of 3 eV is relatively small, making the finite-difference estimate more

sensitive to numerical uncertainty. The associated relative uncertainties are approximately 9–26% in the compressive regime, compared with 2–6% under tension. Consequently, the quantitative interpretation of the decomposition is more accurate on the tensile branch, where the separation between the two correlation treatments is larger. Moreover, because the two branches were relaxed separately, their geometries are nearly but not strictly identical (Section 2.1), so a small geometric contribution to the difference between them cannot be excluded. Other factors, such as strain-induced changes in the Mn 3d–Te 5p hybridisation or exchange pathways beyond the second shell, may also contribute to the strain dependence of the exchange and are not resolved separately in the present analysis.

Having identified the growth of the effective antiferromagnetic contribution as the dominant feature of the tensile response, we next examine its possible structural origin. A simple bond-length-controlled overlap mechanism does not reproduce the calculated trend. Within the adopted superexchange scaling, $|J_{\mathrm{AFM}}|U \propto t^2$, and a conventional distance-dependent description of the hopping amplitude predicts that this contribution should weaken as the Mn–Te bond length increases. The extracted antiferromagnetic contribution instead grows in magnitude under tension, implying that the bond length is not the primary structural parameter controlling it.

The bond angle yields a markedly different result. In the GKA picture, exchange through the ligand-mediated antiferromagnetic pathway is suppressed near 90° and grows as the angle departs from it, with a leading $\cos^2\theta$ dependence [14–17]. On the tensile branch, the angle increases from 93.30° to 97.00°, so that $\cos^2\theta$ increases from 3.3×10^{-3} to 1.49×10^{-2}; over the same interval the magnitude of the extracted antiferromagnetic contribution nearly doubles, and S^2J_{AFM} varies almost linearly with $\cos^2\theta$, with $r = -0.997$ (Figure 4b). This result is remarkable because the same dependence is not apparent in the total J_1, which increases with the angle on the compressive branch but decreases with it on the tensile branch (Figure 5a,b). Microscopically, at $\theta = 90°$ the two Mn–Te σ bonds of a bridging Te ion involve orthogonal Te p orbitals, so that kinetic antiferromagnetic exchange through a common ligand orbital is suppressed; as θ increases, both Mn ions overlap with the same Te p orbital, which opens the antiferromagnetic channel with a strength proportional to $\cos^2\theta$ [16,17]. Under tension, this angular opening outweighs the weaker hopping associated with the longer Mn–Te bonds.

The compressive branch is less clear-cut. There the magnitude of S^2J_{AFM} decreases monotonically towards its minimum at zero strain, while S^2J_{FM} is largest at −3% to −2%; between −2% and 0%, J_1 decreases because J_{FM} decreases slightly faster than $|J_{\mathrm{AFM}}|$. Given the larger uncertainties of the decomposition under compression, the position of the J_1 maximum cannot be attributed to a single contribution from the data alone. Within the phenomenological description, the strain response of the antiferromagnetic contribution can nevertheless be represented by a combination of a short-range term depending on the Mn–Mn separation and the angular term identified above, which vary in opposite directions with strain (Figure 4c). Their crossover occurs near +1.5%, and the magnitude of their sum passes through a shallow minimum near −1.0%, close to the strain at which J_1 is maximal. The statistical comparison over the full strain range favours including both terms. A distance-only model gives a reduced χ^2 of 25.6, an angle-only model with a constant offset gives 1.54, and the combined model gives 0.30 (Figure 4d). Because the combined model contains one additional parameter, the comparison with the angle-only model was also assessed with criteria that penalise model complexity: the combined model lowers the corrected Akaike information criterion by 7.5 and the Bayesian information criterion by 9.0, and an F-test for the additional term gives $p \approx 3 \times 10^{-4}$. If the uncertainties are increased by a factor of 1.5, as suggested by the scatter of the branch difference (Section 2.2), the corresponding reductions fall to 1.1 and 2.7, so the preference for the combined model then

becomes marginal. The need for the distance-dependent term is therefore suggested, but not firmly established, by the present data.

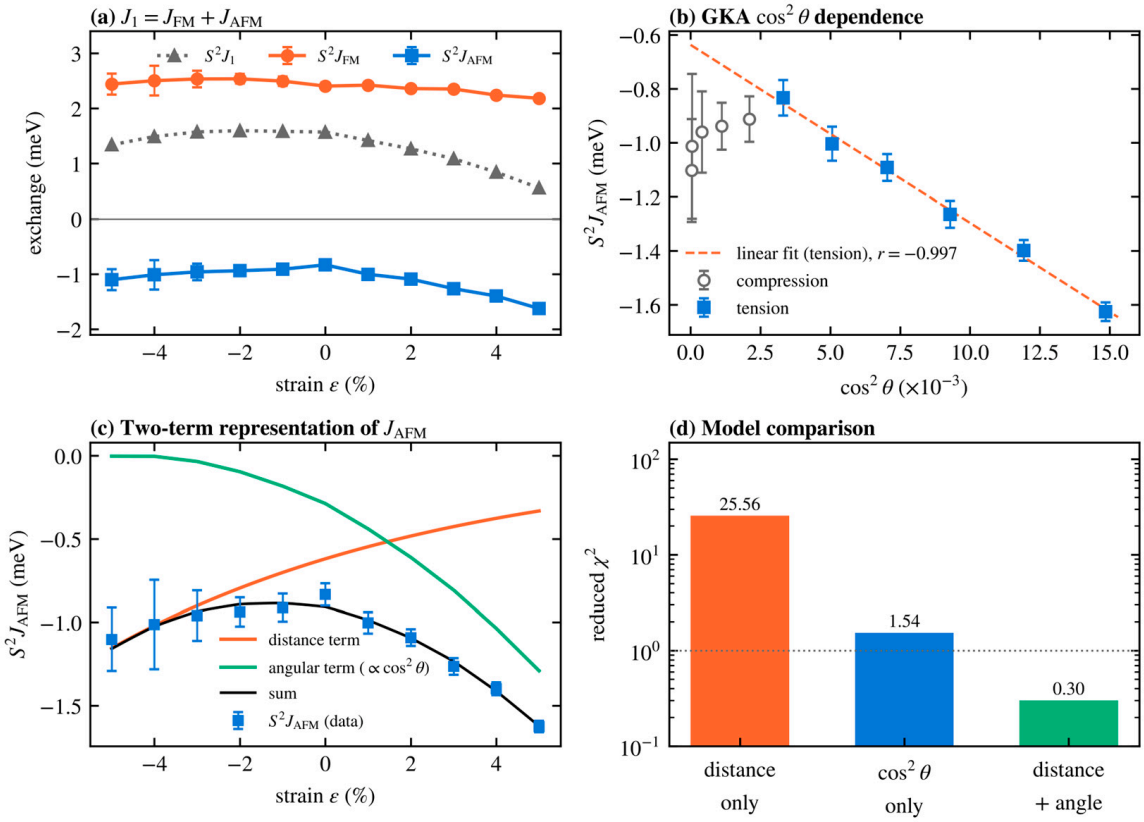


Figure 4. Correlation-sensitive analysis of competing exchange contributions in monolayer $MnSb_2Te_4$. (**a**) Phenomenological decomposition $J_1 = J_{FM} + J_{AFM}$, with $J_{AFM} < 0$, inferred from the U-dependence of the nearest-neighbour exchange. (**b**) S^2J_{AFM} as a function of $\cos^2\theta$; open symbols, compressive branch; filled symbols and dashed line, tensile branch and its linear fit. (**c**) Two-term representation of S^2J_{AFM} by a distance-dependent and an angular ($\propto \cos^2\theta$) term, fitted to all strains. (**d**) Reduced χ^2 of the distance-only, angle-only, and combined models. The dotted horizontal line marks the reference value of reduced $\chi^2 = 1$. Error bars propagate an uncertainty of 0.002 meV in each S^2J_1.

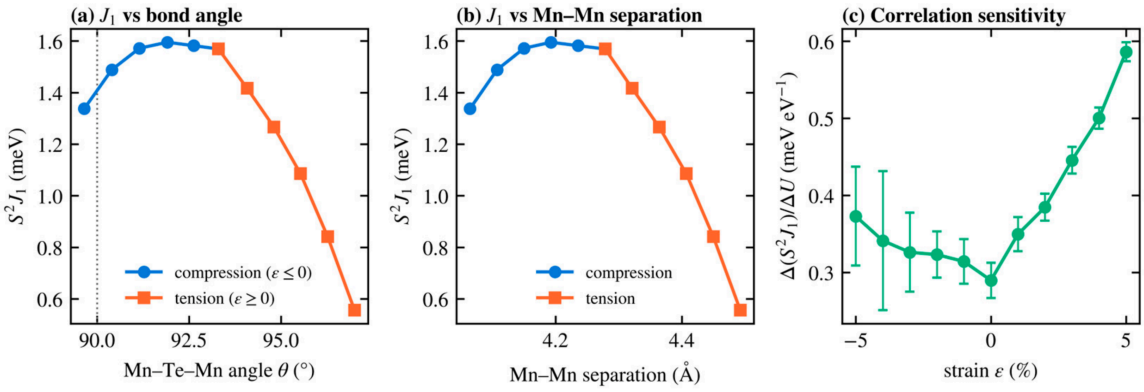


Figure 5. Limitations of single-variable descriptions of the nearest-neighbour exchange interaction. (**a**) S^2J_1 as a function of the Mn–Te–Mn bond angle, showing opposite trends on the compressive and tensile branches, so that the total exchange is not a monotonic function of the angle; the dotted line marks 90°. (**b**) The same comparison for the Mn–Mn separation. (**c**) Correlation sensitivity $\Delta(S^2J_1)/\Delta U$, estimated from the difference between the linear-response and fixed-U calculations; error bars propagate an uncertainty of 0.002 meV in each S^2J_1.

The short-range term is compatible with a rapidly varying distance-dependent contribution, and its fitted decay length of approximately 0.35 Å is short enough to be consistent with direct exchange between neighbouring Mn^{2+} ions. However, its microscopic identity cannot be established from the present data, nor do these data demonstrate that only two microscopic channels exist. The fitted distance and angle variables are themselves strongly correlated because both vary almost linearly with biaxial strain, with parameter correlations reaching $|r| \approx 0.91$. The decomposition should therefore be regarded as a phenomenological separation constrained by the correlation dependence and the observed angular scaling, rather than as a unique microscopic partition. A clean separation would require an additional structural degree of freedom, such as uniaxial strain or constrained geometries in which the bond length and bond angle are varied independently.

One conclusion nevertheless does not depend on assigning a unique microscopic identity to every fitted term. The non-monotonicity of J_1 arises because contributions with different strain dependences compete: on the tensile branch, the ferromagnetic contribution remains comparatively stable, while the magnitude of the antiferromagnetic contribution grows and follows the expected GKA angular dependence. The tensile suppression of J_1, and very probably its maximum, therefore, emerge from the changing balance between competing exchange contributions rather than from an anomalous extremum in a single structural parameter.

3.4. Strain Dependence of Magnetic Ordering

The strain-induced reorganisation of the exchange interactions has direct consequences for the finite-temperature magnetic behaviour of monolayer $MnSb_2Te_4$. To examine this connection, the calculated exchange parameters were used in classical Monte Carlo simulations in both the Ising limit and the anisotropic Heisenberg model described in Section 2.4; the latter, which includes the easy-axis single-ion anisotropy required for finite-temperature order in two dimensions [29,30], provides the physically relevant estimate.

The ordering temperatures of the anisotropic Heisenberg model range from 5.7 to 13.8 K across the investigated strain interval (Figure 6a). They are consistently lower than the corresponding Ising estimates, as expected for a system with finite rather than infinitely strong easy-axis anisotropy. The ratio between the two estimates increases from 0.24 at −5% to 0.34 at +5% (Figure 6b). Because the anisotropy is held fixed, this variation does not originate from the anisotropy; it indicates that the Heisenberg model, whose transverse fluctuations are softened by the competing interaction, responds more strongly to exchange competition than the Ising limit, most clearly at −5%, where the isotropic exchange is close to its stability limit (see below). Varying the anisotropy magnitude supports the same conclusion: halving or doubling D changes T_C by 6–12% at the three strains examined, without altering the strain dependence (Figure 6c). The anisotropy is thus included explicitly in the Monte Carlo Hamiltonian but is held fixed with strain (Section 2.5). A strain dependence of the anisotropy could therefore modify the absolute ordering temperatures and may also affect the detailed strain dependence of T_C. Nevertheless, the non-monotonic trend is also observed in the Ising limit (Figure 6a).

The exchange competition also affects the stability of the magnetic configuration at strong compression. For classical spins on the triangular lattice, the collinear ferromagnetic state of the isotropic two-shell model is stable only for $J_2/J_1 > -1/3$, where the spin stiffness, proportional to $J_1 + 3J_2$, is positive. At −5% strain, $|J_2/J_1|$ reaches 0.343 in the $U(\varepsilon)$ branch, slightly beyond this limit, and the most favourable long-wavelength spiral lies only about 1.5×10^{-3} meV per spin below the ferromagnetic state; in the fixed-U branch, $|J_2/J_1| = 0.327$ and the ferromagnetic state remains stable. With the easy-axis anisotropy included, a spiral with its rotation plane containing the easy axis costs $D/2 = 0.08$ meV

per spin, more than fifty times the exchange energy gained, so the ferromagnetic state is restored within the adopted model. The proximity to the stability limit nevertheless indicates an unusually soft exchange landscape at the strongest compression, in which competing interactions strongly influence low-energy magnetic fluctuations.

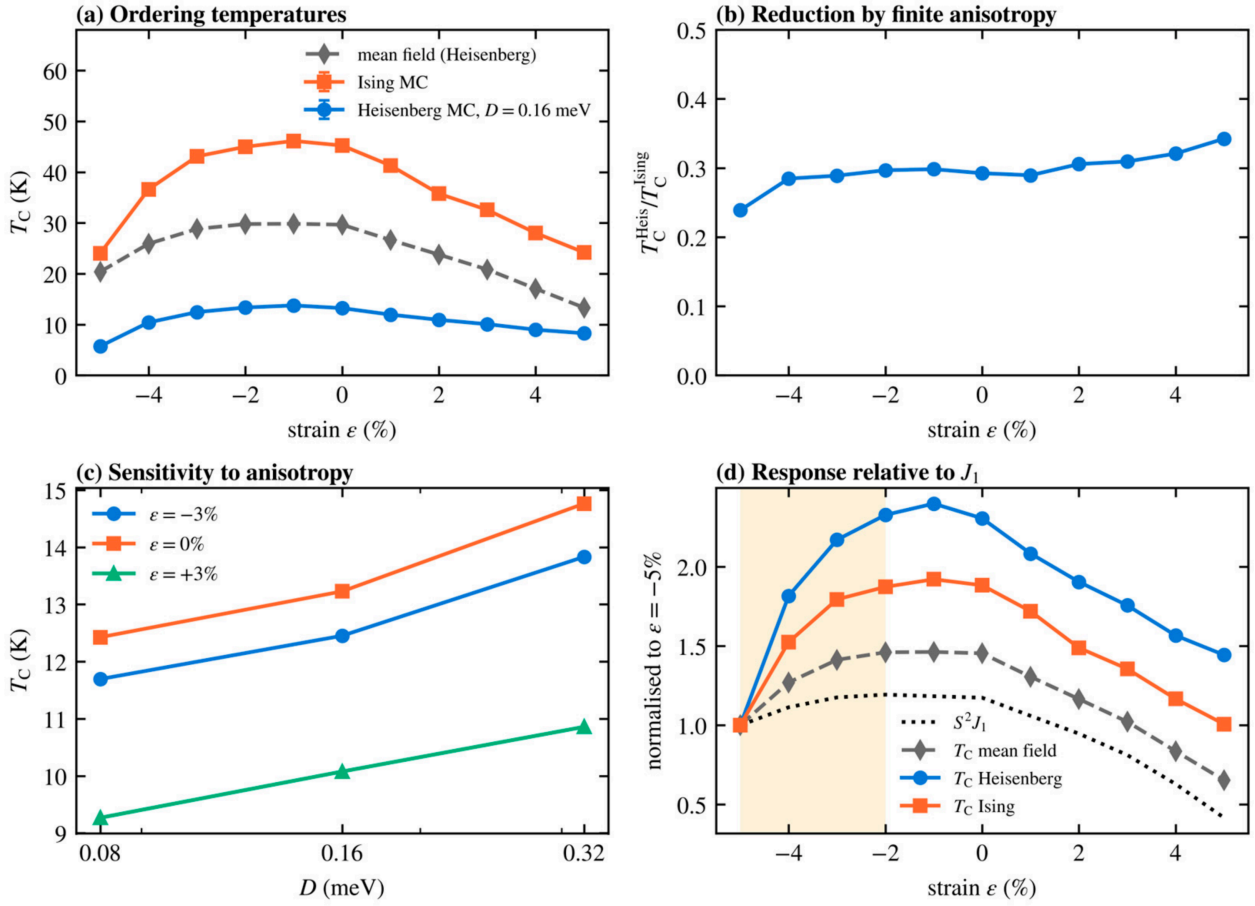


Figure 6. Strain-dependent magnetic ordering governed by the exchange hierarchy in monolayer $MnSb_2Te_4$. (**a**) Ordering temperatures from classical mean-field theory, the Ising limit, and Monte Carlo simulations of the anisotropic Heisenberg model (D = 0.16 meV), obtained from Binder-cumulant crossings (L = 24 and 48); error bars show half the difference between two seeds. (**b**) Ratio of the anisotropic Heisenberg ordering temperature to the corresponding Ising estimate. (**c**) Sensitivity of the Heisenberg ordering temperature to the single-ion anisotropy at three strains. (**d**) Nearest-neighbour exchange and the three ordering-temperature estimates normalised to their values at −5%; in the shaded window (−5% to −2%) every estimate of T_C changes faster than J_1.

Because the exchange landscape is soft at −5%, the ordering at this strain was also checked for metastability. Cooling from a random configuration and heating from the ordered state give the same magnetisation curve within statistical uncertainty for L = 48, so the ordering temperature at this strain is not affected by trapping in multidomain configurations in the present simulations.

The central result is that the ordering temperature does not follow the nearest-neighbour exchange interaction alone (Figure 6d). The anisotropic Heisenberg T_C is largest near −1% and nearly constant between −2% and 0%. Between −5% and −2% strain, the calculated S^2J_1 increases by 19%, from 1.337 to 1.595 meV, whereas T_C rises by 133%, from 5.7 to 13.3 K. This much stronger temperature response coincides with a substantial reduction in the relative strength of the competing effective next-nearest-neighbour interaction, with $|J_2/J_1|$ decreasing from 0.343 to 0.195. Thus, the enhancement of magnetic ordering under

moderate compression is associated with two simultaneous changes: strengthening of the dominant ferromagnetic J_1 interaction and weakening of the competing J_2 contribution.

The comparison among the nearest-neighbour exchange, mean-field estimates, the anisotropic Heisenberg model, and the Ising limit provides further insight into this behaviour. Over the interval between −5% and −2% strain, all three estimates of the ordering temperature increase more strongly than J_1 (+19%): by 46% in mean-field theory, 133% in the anisotropic Heisenberg model, and 87% in the Ising limit. Mean-field theory, which depends only on the combined exchange scale $J_1 + J_2$, accounts for part of this amplification; the additional enhancement found in both Monte Carlo models, largest in the Heisenberg model, reflects the correlations and soft fluctuations associated with competing interactions.

The comparison with mean-field theory further highlights the importance of magnetic correlations. The classical mean-field estimate exceeds the Heisenberg Monte Carlo ordering temperature throughout the investigated strain range, consistent with the neglect of spatial correlations and fluctuations. Moreover, the ratio of the Monte Carlo to the mean-field ordering temperature decreases systematically as the competition ratio increases, with $r = -0.995$. This correlation provides additional evidence that the effective next-nearest-neighbour interaction influences not only the relative energies of the collinear configurations but also the collective fluctuations governing magnetic ordering.

The absolute ordering temperatures should be interpreted within the scope of the model (Section 2.5). Experimental $MnSb_2Te_4$ samples are generally bulk, epitaxial, or multilayer systems, in which interlayer coupling, Mn/Sb site mixing, and sample-dependent structural conditions influence the magnetic response [8–10]. The calculated values therefore represent a clean-limit reference for an isolated monolayer rather than predictions for a particular experimental specimen.

4. Conclusions

This study demonstrates that biaxial strain significantly reorganises the hierarchy of competing exchange interactions in monolayer $MnSb_2Te_4$. Although the structural geometry and local electronic descriptors evolve smoothly, the nearest-neighbour ferromagnetic interaction shows a complex behaviour: it rises by about 19% under compression from −5% to −2%, remains nearly constant between −2% and 0%, and falls by 65% under tension up to +5%. In contrast, the effective next-nearest-neighbour interaction is progressively suppressed and eventually changes sign, reducing $|J_2/J_1|$ from 0.34 to 0.03 over the studied strain range. These contrasting trends establish that the strain-dependent magnetic behaviour cannot be adequately described by a single exchange parameter or inferred directly from an individual structural or electronic descriptor.

By comparing DFT + U calculations performed at nearly identical geometries with linear-response and fixed Hubbard parameters, we identified, within a phenomenological description, competing distance- and angle-dependent contributions to the net nearest-neighbour exchange that vary in opposite directions with strain and produce its complex behaviour; the growing antiferromagnetic contribution on the tensile branch follows the $\cos^2\theta$ dependence expected for ligand-mediated superexchange in the Goodenough–Kanamori–Anderson framework [14–17]. The analysis shows that correlation sensitivity is a useful probe of competing contributions obscured in the total exchange interaction, although individual microscopic exchange pathways cannot be uniquely distinguished.

Classical Monte Carlo simulations incorporating easy-axis single-ion anisotropy further demonstrate that the competing evolution of the dominant nearest-neighbour exchange and its next-nearest-neighbour counterpart leads to a non-monotonic strain dependence of the magnetic ordering temperature. The ordering temperature increases by about 133% between −5% and −2%, whereas the nearest-neighbour exchange increases by only 19%; it

then shows a flat maximum between −2% and 0% and is suppressed under tension, by about 37% at +5% relative to the unstrained monolayer. The calculated ordering temperatures should be interpreted as clean-limit estimates for an ideal isolated monolayer, given that interlayer coupling and chemical disorder are not included in the present model.

Beyond $MnSb_2Te_4$, these findings have two broader implications for computational studies of low-dimensional magnets. First, comparing DFT + U calculations at nearly identical geometries but with different Hubbard parameters can provide a practical tool for analysing competing exchange contributions with distinct correlation dependences. Second, they provide a microscopic basis for understanding complex strain-engineered magnetism in two-dimensional materials, through the relationship between the responses of multiple contributions to the overall magnetic interaction and the variation in structural parameters. The approach is expected to be most reliable for magnets with localised moments and ligand-mediated exchange. In itinerant magnets, where the exchange is mediated by conduction electrons and the magnitude of the local moments is strongly coupled to the lattice, as illustrated by the super-Invar behaviour of $R_2(Fe,Co)_{17}$ compounds [34] and the giant negative thermal expansion of a kagome ferromagnet [35], the U-dependence of the exchange cannot be interpreted solely in terms of a kinetic antiferromagnetic contribution, and the present decomposition is not directly applicable. In systems with strong spin–orbit coupling or strongly competing interactions, anisotropic exchange and further-neighbour couplings would also need to be included explicitly.

Author Contributions: Conceptualization, T.-A.T.; methodology, T.-A.T. and N.T.D.; software, T.-A.T. and L.V.T.N.; validation, N.T.D. and D.P.K.; formal analysis, T.-A.T., L.V.T.N. and S.H.L.; investigation, L.V.T.N., S.H.L. and H.C.T.; resources, N.L.P. and D.P.K.; data curation, L.V.T.N. and H.C.T.; writing—original draft preparation, T.-A.T.; writing—review and editing, N.T.D., N.L.P. and D.P.K.; visualization, S.H.L. and H.C.T.; supervision, T.-A.T.; project administration, T.-A.T.; funding acquisition, T.-A.T. All authors have read and agreed to the published version of the manuscript.

Funding: This research was funded by Ho Chi Minh City University of Technology and Engineering, grant number T2025-02NTĐ.

Institutional Review Board Statement: Not applicable.

Informed Consent Statement: Not applicable.

Data Availability Statement: Data will be made available on request.

Acknowledgments: The DFT calculations were performed on the high-performance computing cluster at Ho Chi Minh City University of Education, Vietnam.

Conflicts of Interest: The authors declare no conflicts of interest.

References

1. Burch, K.S.; Mandrus, D.; Park, J.-G. Magnetism in two-dimensional van der Waals materials. *Nature* **2018**, *563*, 47–52. [CrossRef]
2. Gong, C.; Zhang, X. Two-dimensional magnetic crystals and emergent heterostructure devices. *Science* **2019**, *363*, eaav4450. [CrossRef]
3. Webster, L.; Yan, J.-A. Strain-tunable magnetic anisotropy in monolayer $CrCl_3$, $CrBr_3$, and CrI_3. *Phys. Rev. B* **2018**, *98*, 144411.
4. Cenker, J.; Sivakumar, S.; Xie, K.; Miller, A.; Thijssen, P.; Liu, Z.; Dismukes, A.; Fonseca, J.; Anderson, E.; Zhu, X.; et al. Reversible strain-induced magnetic phase transition in a van der Waals magnet. *Nat. Nanotechnol.* **2022**, *17*, 256–261. [CrossRef]
5. Li, J.; Li, Y.; Du, S.; Wang, Z.; Gu, B.-L.; Zhang, S.-C.; He, K.; Duan, W.; Xu, Y. Intrinsic magnetic topological insulators in van der Waals layered $MnBi_2Te_4$-family materials. *Sci. Adv.* **2019**, *5*, eaaw5685. [CrossRef]
6. Zhang, D.; Shi, M.; Zhu, T.; Xing, D.; Zhang, H.; Wang, J. Topological axion states in the magnetic insulator $MnBi_2Te_4$ with the quantized magnetoelectric effect. *Phys. Rev. Lett.* **2019**, *122*, 206401. [CrossRef]

7. Klimovskikh, I.I.; Otrokov, M.M.; Estyunin, D.; Eremeev, S.V.; Filnov, S.O.; Koroleva, A.; Shevchenko, E.; Voroshnin, V.; Rybkin, A.G.; Rusinov, I.P.; et al. Tunable 3D/2D magnetism in the $(MnBi_2Te_4)(Bi_2Te_3)_m$ topological insulators family. *npj Quantum Mater.* **2020**, *5*, 54. [CrossRef]
8. Murakami, T.; Nambu, Y.; Koretsune, T.; Gu, X.; Yamamoto, T.; Brown, C.M.; Kageyama, H. Realization of interlayer ferromagnetic interaction in $MnSb_2Te_4$ toward the magnetic Weyl semimetal state. *Phys. Rev. B* **2019**, *100*, 195103. [CrossRef]
9. Liu, Y.; Wang, L.-L.; Zheng, Q.; Huang, Z.; Wang, X.; Chi, M.; Wu, Y.; Chakoumakos, B.C.; McGuire, M.A.; Sales, B.C.; et al. Site mixing for engineering magnetic topological insulators. *Phys. Rev. X* **2021**, *11*, 021033. [CrossRef]
10. Yan, D.Y.; Yang, M.; Song, P.B.; Song, Y.T.; Wang, C.X.; Yi, C.J.; Shi, Y.G. Site mixing induced ferrimagnetism and anomalous transport properties of the Weyl semimetal candidate $MnSb_2Te_4$. *Phys. Rev. B* **2021**, *103*, 224412. [CrossRef]
11. Li, B.; Yan, J.-Q.; Pajerowski, D.M.; Gordon, E.; Nedić, A.-M.; Sizyuk, Y.; Ke, L.; Orth, P.P.; Vaknin, D.; McQueeney, R.J. Competing magnetic interactions in the antiferromagnetic topological insulator $MnBi_2Te_4$. *Phys. Rev. Lett.* **2020**, *124*, 167204. [CrossRef]
12. Ahn, J.; Ghosh, S.; Kang, S.-H.; Jeong, D.; Eisenbach, M.; Kwon, Y.-K.; Reboredo, F.A.; Krogel, J.T.; Yoon, M. Optimizing density functional theory for strain-dependent magnetic properties of monolayer $MnBi_2Te_4$ with diffusion Monte Carlo. *2D Mater.* **2026**, *13*, 045011. [CrossRef]
13. Cococcioni, M.; de Gironcoli, S. Linear response approach to the calculation of the effective interaction parameters in the LDA+U method. *Phys. Rev. B* **2005**, *71*, 035105. [CrossRef]
14. Anderson, P.W. New approach to the theory of superexchange interactions. *Phys. Rev.* **1959**, *115*, 2. [CrossRef]
15. Anderson, P.W. Theory of magnetic exchange interactions: Exchange in insulators and semiconductors. In *Solid State Physics*; Seitz, F., Turnbull, D., Eds.; Academic Press: New York, NY, USA, 1963; Volume 14, pp. 99–214.
16. Goodenough, J.B. Theory of the role of covalence in the perovskite-type manganites [La, M(II)]MnO_3. *Phys. Rev.* **1955**, *100*, 564. [CrossRef]
17. Kanamori, J. Superexchange interaction and symmetry properties of electron orbitals. *J. Phys. Chem. Solids* **1959**, *10*, 87–98. [CrossRef]
18. Giannozzi, P.; Baroni, S.; Bonini, N.; Calandra, M.; Car, R.; Cavazzoni, C.; Ceresoli, D.; Chiarotti, G.L.; Cococcioni, M.; Dabo, I.; et al. QUANTUM ESPRESSO: A modular and open-source software project for quantum simulations of materials. *J. Phys. Condens. Matter* **2009**, *21*, 395502. [CrossRef]
19. Giannozzi, P.; Andreussi, O.; Brumme, T.; Bunau, O.; Buongiorno Nardelli, M.; Calandra, M.; Car, R.; Cavazzoni, C.; Ceresoli, D.; Cococcioni, M.; et al. Advanced capabilities for materials modelling with Quantum ESPRESSO. *J. Phys. Condens. Matter* **2017**, *29*, 465901. [CrossRef]
20. Perdew, J.P.; Burke, K.; Ernzerhof, M. Generalized gradient approximation made simple. *Phys. Rev. Lett.* **1996**, *77*, 3865. [CrossRef]
21. Dal Corso, A. Pseudopotentials periodic table: From H to Pu. *Comput. Mater. Sci.* **2014**, *95*, 337–350. [CrossRef]
22. Grimme, S.; Antony, J.; Ehrlich, S.; Krieg, H. A consistent and accurate ab initio parametrization of density functional dispersion correction (DFT-D) for the 94 elements H-Pu. *J. Chem. Phys.* **2010**, *132*, 154104.
23. Dudarev, S.L.; Botton, G.A.; Savrasov, S.Y.; Humphreys, C.J.; Sutton, A.P. Electron-energy-loss spectra and the structural stability of nickel oxide: An LSDA+U study. *Phys. Rev. B* **1998**, *57*, 1505. [CrossRef]
24. Zhou, L.; Tan, Z.; Yan, D.; Fang, Z.; Shi, Y.; Weng, H. Topological phase transition in the layered magnetic compound $MnSb_2Te_4$: Spin-orbit coupling and interlayer coupling dependence. *Phys. Rev. B* **2020**, *102*, 085114. [CrossRef]
25. Sohier, T.; Calandra, M.; Mauri, F. Density functional perturbation theory for gated two-dimensional heterostructures: Theoretical developments and application to flexural phonons in graphene. *Phys. Rev. B* **2017**, *96*, 075448. [CrossRef]
26. Henkelman, G.; Arnaldsson, A.; Jónsson, H. A fast and robust algorithm for Bader decomposition of charge density. *Comput. Mater. Sci.* **2006**, *36*, 354–360. [CrossRef]
27. Sanville, E.; Kenny, S.D.; Smith, R.; Henkelman, G. Improved grid-based algorithm for Bader charge allocation. *J. Comput. Chem.* **2007**, *28*, 899–908. [CrossRef]
28. Tang, W.; Sanville, E.; Henkelman, G. A grid-based Bader analysis algorithm without lattice bias. *J. Phys. Condens. Matter* **2009**, *21*, 084204. [CrossRef]
29. Mermin, N.D.; Wagner, H. Absence of ferromagnetism or antiferromagnetism in one- or two-dimensional isotropic Heisenberg models. *Phys. Rev. Lett.* **1966**, *17*, 1133–1136. [CrossRef]
30. Torelli, D.; Olsen, T. Calculating critical temperatures for ferromagnetic order in two-dimensional materials. *2D Mater.* **2019**, *6*, 015028. [CrossRef]
31. Li, Y.; Jiang, Z.; Li, J.; Xu, S.; Duan, W. Magnetic anisotropy of the two-dimensional ferromagnetic insulator $MnBi_2Te_4$. *Phys. Rev. B* **2019**, *100*, 134438. [CrossRef]
32. Pakdel, S.; Olsen, T.; Thygesen, K.S. Effect of Hubbard U corrections on the electronic and magnetic properties of 2D materials: A high-throughput study. *npj Comput. Mater.* **2025**, *11*, 18. [CrossRef]
33. Wines, D.; Saritas, K.; Ataca, C. The intrinsic ferromagnetism of two-dimensional (2D) MnO_2 revisited: A many-body quantum Monte Carlo and DFT+U study. *J. Phys. Chem. C* **2022**, *126*, 5813–5821. [CrossRef]

34. Cao, Y.; Lin, K.; Khmelevskyi, S.; Avdeev, M.; Taddei, K.M.; Zhang, Q.; Huang, Q.; Li, Q.; Kato, K.; Tang, C.C.; et al. Ultrawide temperature range super-Invar behavior of $R_2(Fe,Co)_{17}$ materials (R = rare earth). *Phys. Rev. Lett.* **2021**, *127*, 055501. [CrossRef]
35. Zhou, H.; Cao, Y.; Khmelevskyi, S.; Hu, S.; Lin, K.; Zhang, T.; Xing, X. Realization of giant negative thermal expansion via a significantly decreased local moment in a kagome ferromagnet with spin reorientation. *J. Am. Chem. Soc.* **2026**, *148*, 32210–32218. [CrossRef]

Disclaimer/Publisher's Note: The statements, opinions and data contained in all publications are solely those of the individual author(s) and contributor(s) and not of MDPI and/or the editor(s). MDPI and/or the editor(s) disclaim responsibility for any injury to people or property resulting from any ideas, methods, instructions or products referred to in the content.